Theoretical aspects of tunneling-current-induced bond excitation and breaking at surfaces

Nicolas Lorente† and Mats Persson

Department of Applied Physics, Chalmers/Göteborg University, S-41296 Göteborg, Sweden

Received 7th April 2000
First published as an Advance Article on the web 4th October 2000

We have performed a density functional study of the electronic structure, images and vibrationally inelastic tunneling in the scanning tunneling microscope and vibrational damping by excitation of electron–hole pairs of CO chemisorbed on the (111) and (100) faces of Cu. We find that the $2\pi^*$ molecular orbital of CO turns into a broad resonance with parameters that differ significantly from those suggested by inverse and two-photon photoemission measurements. The calculated vibrational damping rate for the internal stretch mode and relative changes in tunneling conductance across vibrational thresholds are in agreement with experiment. The non-adiabatic electron–vibration coupling is well described by the Newn–Anderson model for the $2\pi^*$-derived resonance whereas this model is not able to describe the non-adiabatic coupling between the tunneling electrons and the vibration. We believe that this model misses an important mechanism for vibrational excitation in tunneling that involves the change of tunneling amplitude by deformation of the tails of the one-electron wavefunctions with vibrational coordinate.

I. Introduction

The unique ability of the scanning tunneling microscope (STM) to manipulate and characterize single molecules on surfaces by inelastic electron tunneling provides new understanding and control of the surface chemical bond and reactivity.[1] The highly localized inelastic electron tunneling in space, has made it possible to desorb single atoms,[2,3] to dissociate single diatomic molecules,[4] to break single bonds in polyatomic molecules,[5] to form new bonds by transferring atoms and molecules, reversibly, to and from the tip,[6–8] induce reversible rotational motion[9,10] and perform vibrational microscopy.[11]

Most theoretical attempts to describe and understand bond excitation and breaking by inelastic electron tunneling are based on a resonance model for the adsorbate-induced electronic structure and the non-adiabatic electron–vibration coupling.[3,7,12–15] This model, that involves the coupling to a local vibrational mode, has a long history and has been applied to various electronically non-adiabatic processes such as: desorption induced by electronic transitions and driven by laser-excited hot electrons,[16] vibrational damping by excitation of electron–hole pairs,[17] and vibrationally inelastic tunneling.[18] In the resonance model, an adsorbate-induced antibonding state is temporarily occupied by a tunneling electron, resulting in a motion of the nuclear wave packet on the excited-state potential until the resonance decays, after which the wave packet is no longer

† Permanent address: Laboratoire Collisions Agrégats Réactivité, UMR 5589, Université Paul Sabatier, 31062 Toulouse Cedex, France.

exclusively in the lowest vibrational state and can even escape by ending up in a state above the barrier. This model has been used to rationalize observed power-law dependence on the tunneling current of the transfer rate in the atomic switch,[12,13,15] the desorption rate of H on Si(100),[3] and the dissociation rate of O_2 on Pt(111)[4] and involves, typically, a number of adjustable parameters, with the notable exception of the treatment by Stokbro and coworkers[3] where the parameters were determined from density functional calculations.

The recent development of vibrational spectroscopy and microscopy by inelastic electron tunneling[11] has made it possible to study the non-adiabatic coupling between tunneling electrons and vibrations in more detail. We have recently developed a theory of vibrationally inelastic tunneling based on density functional theory (DFT) and a generalization of Tersoff–Hamann (TH) theory. Using this theory we were able to calculate STM images for C_2H_2 chemisorbed on Cu(100) and relative changes in tunneling conductance across vibrational modes and their spatial images that were in good agreement with experiment.[19] CO on Cu provides a most interesting system to study the nature of the electron–vibration coupling in tunneling-current-induced bond excitation and breaking at surfaces and in vibrational damping by electron–hole pair excitations because, for this system, the resonance state derived from the $2\pi^*$ molecular orbital of CO has been argued to play an important role in some of these processes and experimental data of these resonance state parameters, tip-induced desorption rates, vibrationally inelastic tunneling efficiencies and vibrational damping rates are available for comparison with theory.

In this paper, we have applied our theory to the calculation of STM images, relative changes in tunneling conductance across vibrational thresholds and vibrational damping rates of CO on the (111) and the (100) faces of Cu. The non-adiabatic electron–vibration interaction was treated by perturbation theory. The one-electron wavefunctions and electron–vibration couplings were calculated in a super-cell geometry using a plane-wave and pseudopotential method. The one-electron structure of the chemisorbed molecule, in particular, the $2\pi^*$-derived state, was characterized by calculating the projected density of states on molecular orbitals. The results are discussed in relation to both available experimental data and results from a resonance model.

The paper is organized as follows. We begin by giving some details of the density functional calculations in Section II A and show in Section II B, how the local density of states (LDOS) in the TH approach to STM images and the projected density of states (PDOS) on molecular orbitals were calculated using density functional calculations. In Section II C, we present expressions for relative changes in vibrational conductance based on a generalization of the TH theory to vibrationally inelastic tunnelling and for vibrational damping rates by excitation of electron–hole pairs and show how these expressions are simplified in the Newns–Anderson model. In addition, we give some details of how these expressions were calculated using the plane-wave, pseudopotential method. We present our results for the $2\pi^*$-derived resonance feature in the PDOS, STM images and vibrationally inelastic tunneling efficiences and vibrational damping rates and discuss them in relation to experimental data in Sections III A, III B and III C, respectively. In Section III D, we discuss our results in relation to the Newns–Anderson model for the $2\pi^*$-derived states and tip-induced desorption experiments and, finally, in Section III D give a short summary and some concluding remarks.

II. Theory

A. Some details of the density functional calculations

The chemisorption and one-electron structure calculations were based on DFT and performed using the plane-wave pseudopotential code DACAPO.[20] The exchange-correlation effects were described by the PW91 version of the generalized gradient approximation (GGA).[21]

The (111) and (100) surfaces of Cu were represented by slabs in a super cell geometry. We used slabs of various sizes, which included 2×2, 3×3 and 4×4 surface unit cells and 4 to 6 layers of Cu atoms. The vacuum region of the (111) and (100) slabs contained 4 and 5 layers, respectively. The CO molecule was only adsorbed on one side of the slab and the net surface dipole moment was compensated by a dipole layer and an energy correction term.[22] The scattering of the valence electrons from the C, O and Cu ion-cores were represented by ultrasoft pseudopotentials that allowed a plane-wave cut-off energy of 25 Ry. The surface Brillouin zones were sampled using a

uniform two-dimensional mesh with a constant density of k points for the various surface unit cells.[23] The geometry of the adsorbed CO molecule was optimized using a quasi-Newton method where ionic forces were obtained from the converged electron density using Hellman–Feynman theorem. The ionic forces were also used in the construction of the dynamical matrix for the calculation of vibrational modes.

B. Local and projected density of states

In this section we give a short account of the TH theory of STM images in terms of LDOS and show how the LDOS and the PDOS on molecular orbitals have been calculated using the plane-wave, pseudopotential method in a super cell geometry.

Our calculations of the STM images are based on the TH theory[24] and involve calculation of the LDOS at the Fermi level. This theory is based on an independent electron approximation, the Bardeen approximation for the tunneling matrix element, and an s-wave representation of the tip electronic structure. At zero temperature and low tip–sample bias, V, the differential conductance, $\mathrm{d}I/\mathrm{d}V$, is then simply related to the LDOS, $\rho(\boldsymbol{r}_0, \varepsilon)$, as

$$\frac{\mathrm{d}I}{\mathrm{d}V}(V) \propto \rho(\boldsymbol{r}_0, \varepsilon_\mathrm{F} + eV) = \sum_\alpha |\psi_\alpha(\boldsymbol{r}_0)|^2 \delta(\varepsilon_\mathrm{F} + eV - \varepsilon_\alpha) \quad (1)$$

where $\boldsymbol{r}_0$ is the location of the tip apex, ε_F the Fermi energy of the sample. In the second step, we have expanded the LDOS in one-electron wavefunctions $\psi_\alpha(\boldsymbol{r})$ and energies ε_α. Another related quantity that provides useful information about the electronic structure is the PDOS on an orbital $\psi_\mathrm{a}(\boldsymbol{r})$ defined as,

$$\rho_\mathrm{a}(\varepsilon) = \sum_\alpha |\langle \psi_\alpha | \psi_\mathrm{a} \rangle|^2 \delta(\varepsilon - \varepsilon_\alpha). \quad (2)$$

Note that $\rho_\mathrm{a}(\varepsilon)$ obeys the sum rule that it should integrate up to unity.

The calculation of the LDOS and PDOS using the plane-wave and ultrasoft pseudopotential (US-PP) method in a supercell geometry is not entirely straightforward. In the US-PP calculations, the pseudo wavefunctions, $\tilde{\psi}(\boldsymbol{r})$ are in general labeled by a composite index $\alpha = (n, \boldsymbol{k}_\parallel)$ that includes the band index, n and the wavevector $\boldsymbol{k}_\parallel$ in the surface Brillouin zone. These wavefunctions form only an orthonormal set when introducing the so-called overlap matrix $\hat{S}$ associated with the ultrasoft pseudopotentials.[25] So we calculated the matrix element in eqn. (2) from the states $|\psi_\mathrm{a}\rangle = \hat{S}^{1/2}|\tilde{\psi}_\mathrm{a}\rangle$ and $|\psi_\alpha|\rangle = \hat{S}^{1/2}|\tilde{\psi}_\alpha\rangle$ that we have constructed by calculating $\hat{S}^{1/2}$ and its action on the pseudo-states.[26] In the expression for the LDOS in eqn. (1), we can use directly the pseudo-wavefunctions $\tilde{\psi}_\alpha(\boldsymbol{r}_0)$ because $\boldsymbol{r}_0$ is far outside the ion cores but, as pointed out in earlier works,[27] we need to extrapolate analytically the tails of the wavefunctions to the tip region. An additional calculational aspect is that the finite set of k points and the finite slab thickness in PP calculations make the spectrum of one-electron states discrete. We handled this aspect by introducing a Gaussian broadening of the δ function in eqn. (2) as

$$\delta(\varepsilon) \rightarrow \frac{\exp\left(-\frac{\varepsilon^2}{\sigma^2}\right)}{\sigma\sqrt{\pi}} \quad (3)$$

Finally, note that the periodicity of the super cell makes the sums in eqn. (1) and (2) diagonal over $\boldsymbol{k}_\parallel$.

C. Vibrationally inelastic tunneling and vibrational damping rates

Here we give a short account of the theory of the change in tunneling conductance across a vibrational mode and excitation of electron–hole pairs by a vibrational mode. We show also how these quantities have been calculated using DFT and the US-PP method in a supercell geometry.

We have calculated the non-adiabatic effects of the adsorbate vibration on the tunneling current using a generalization of the TH expression for the tunneling current in eqn. (1) to include the

electron–vibration coupling in the sample.[28] This generalization states simply that $\rho(\boldsymbol{r}_0; \varepsilon)$ in eqn. (1) should be the LDOS for the electrons interacting with the adsorbate vibration. This interaction is in general weak and can be calculated using the lowest order vibration self-energy diagram in the many-body perturbation expansion of $\rho(\boldsymbol{r}_0; \varepsilon)$.[29] One finds, using this approach, that this coupling results in a discontinuity, $\Delta\rho(\boldsymbol{r}_0)$ of $\rho(\boldsymbol{r}_0; \varepsilon + eV)$ across the threshold, $\varepsilon = \varepsilon_F + \hbar\Omega$, for a vibrational excitation with energy, $\hbar\Omega$, resulting in a discontinuous change, $\Delta\sigma$, of the differential conductance $\sigma = \mathrm{d}I/\mathrm{d}V$. The relative change of this tunneling conductance, $\Delta\sigma/\sigma$ across the vibrational energy is given by,

$$\eta_{\mathrm{tot}}(\boldsymbol{r}_0) = \frac{\Delta\rho(\boldsymbol{r}_0)}{\rho(\boldsymbol{r}_0; \varepsilon_F)}. \tag{4}$$

The discontinuity $\Delta\rho(\boldsymbol{r}_0)$ has two contributions: an inelastic contribution $\Delta\rho_{\mathrm{inel}}(\boldsymbol{r}_0)$, where the vibration is excited by the tunneling electrons in the sample, and an elastic contribution $\Delta\rho_{\mathrm{el}}(\boldsymbol{r}_0)$, which takes into account the elastic effect of the vibration on the tunneling electrons in the sample. From a calculational point of view, we find it convenient to make the following decomposition of these two contributions:

$$\Delta\rho_{\mathrm{inel}}(\boldsymbol{r}_0) = \Delta\rho_P(\boldsymbol{r}_0) + \Delta\rho_I(\boldsymbol{r}_0) \tag{5}$$

$$\Delta\rho_{\mathrm{el}}(\boldsymbol{r}_0) = -2\Delta\rho_I(\boldsymbol{r}_0) \tag{6}$$

where in the quasi-static limit, $\hbar\Omega \to 0$,

$$\Delta\rho_I(\boldsymbol{r}_0) = \delta Q^2 \sum_\beta \left| \pi \sum_\alpha \psi_\alpha(\boldsymbol{r}_0) \langle \psi_\alpha | v' | \psi_\beta \rangle \delta(\varepsilon_\beta - \varepsilon_\alpha) \right|^2 \delta(\varepsilon_F - \varepsilon_\beta) \tag{7}$$

and

$$\Delta\rho_P(\boldsymbol{r}_0) = \sum_\alpha |\delta\psi_\alpha(\boldsymbol{r}_0)|^2 \delta(\varepsilon_F - \varepsilon_\alpha). \tag{8}$$

Here the electron–vibration coupling, v', is the derivative of the effective one-electron potential, v_{eff}, with respect to the vibrational displacement, Q, and $\delta Q^2 = \hbar/(2M\Omega)$ is the mean-square amplitude of Q and M is the mass associated with Q and $\delta\psi_\alpha(\boldsymbol{r}_0)$ is the first-order change in a one-electron wavefunction $\psi_\alpha(\boldsymbol{r}_0)$ when making a static displacement δQ.

Our theory for the relative change in conductance, η, across a vibrational energy, based on the TH approach, assumes that the electron–vibration coupling is restricted to the sample and ignores the contribution to η from the long-range dipole interaction for electrons tunneling between the sample and the tip. This contribution, η_{dip}, can be shown to have no elastic component and is positive.[29] As shown by Persson and coworkers,[18,30] the maximum value of η_{dip} can be estimated by the following simple result,

$$\eta_{\mathrm{dip}}^{\mathrm{max}} = \left(\frac{\delta\mu}{ea_0}\right)^2 \tag{9}$$

where $\delta\mu$ is the root-mean-square amplitude of the dipole moment of the charge distribution and a_0 is the Bohr radius.

The calculation of the damping rate of a vibrational mode by excitations of electron–hole pairs is also based on first-order perturbation theory in the electron–vibration coupling. In the quasi-static limit, $\hbar\Omega \to 0$, the damping rate, γ_{eh}, is given by,[31]

$$\gamma_{\mathrm{eh}} = \frac{2\pi\hbar}{M} \sum_{\alpha,\beta} |\langle \psi_\beta | v' | \psi_\alpha \rangle|^2 \delta(\varepsilon_F - \varepsilon_\beta)\delta(\varepsilon_F - \varepsilon_\alpha), \tag{10}$$

which includes spin degeneracy. Note that γ_{eh} is independent of the vibrational frequency.

In the Newns-Anderson (NA) model of a resonance level coupled to a vibration, we have shown elsewhere[28] that the results for η_{el} and η_{inel} derived from eqn. (4), (6), (8) and (7) and the result for γ_{eh} in eqn. (10) reduce to results derived earlier by Persson and Baratoff[18] for the vibrationally inelastic tunneling probability and by Persson and Persson[17] for the vibrational damping rate, respectively. In this model a single one-electron state $|\psi_a\rangle$ with energy ε_a is interacting with a

continuum of one-electron states and the electron–vibration coupling is assumed to be governed by the slope of ε_a with respect to the vibrational coordinate q. For this particular electron–vibration coupling one finds in the NA model the following results for η_{inel} and γ_{eh}:

$$\eta_{inel}(\boldsymbol{r}_0) = \delta Q^2 \left(\frac{\partial \varepsilon_a}{\partial q}\right)^2 \frac{1}{\Delta\varepsilon_a^2 + \gamma_a^2} \frac{\rho_a(\varepsilon_F)\,|\,\psi_a(\boldsymbol{r}_0)\,|^2}{\rho(\boldsymbol{r}_0\,;\,\varepsilon_F)}\,, \tag{11}$$

and

$$\gamma_{eh} = \frac{2\pi\hbar}{M}\left(\frac{\partial \varepsilon_a}{\partial q}\right)^2 \rho_a(\varepsilon_F)^2. \tag{12}$$

Here $\Delta\varepsilon_a$ and γ_a are defined by the Green function, $g_a(\varepsilon)$, projected on $|\,\psi_a\rangle$ as,

$$g_a(\varepsilon_F) \equiv \frac{1}{\Delta\varepsilon_a + i\gamma_a} \tag{13}$$

and $\rho_a(\varepsilon_F) \equiv -1/\pi$ Im $g_a(\varepsilon_F)$ is the density of states projected on $|\,\psi_a\rangle$. In the case of a simple well-defined resonance, $\Delta\varepsilon_a$ and γ_a are the resonance position with respect to the Fermi level and the half-width at half-maximum, respectively. The last factor in eqn. (11) takes into account that, in general, only a fraction of the electrons tunnel through the adsorbate state $|\,\psi_a\rangle$.

There are several aspects in the evaluation of $\eta_{el}(\boldsymbol{r}_0)$, $\eta_{inel}(\boldsymbol{r}_0)$ and γ_{eh} using the US-PP method in a supercell geometry. A few aspects are common to those in the calculation of the TH expression for the tunneling current in eqn. (1) such as the need to broaden the δ functions in eqn. (7), (8) and (10) by the Gaussian function in eqn. (3) and to extrapolate the wavefunctions to the tip region. In this case the justification for introducing such a broadening is based on the assumption that the variation of the electronic structure on the scale of the vibrational energies is small. The other new aspects involve calculation of the matrix element $\langle\psi_\alpha\,|\,v'\,|\,\psi_\beta\rangle$ in eqn. (7), (10) and the first-order change in the wavefunction, $\delta\psi_\alpha(\boldsymbol{r}_0)$ in eqn. (8). We follow Head-Gordon and Tully[32] and use first order perturbation theory to re-express the matrix element in terms of wavefunction overlaps and one-electron energies as,

$$\langle\psi_{\alpha'}\,|\,\delta v\,|\,\psi_\alpha\rangle = \begin{cases} 0, & \boldsymbol{k}_{\|} \neq \boldsymbol{k}_{\|} \\ \delta\varepsilon_\alpha, & n' = n,\ \boldsymbol{k}_{\|} = \boldsymbol{k}'_{\|} \\ (\varepsilon_\alpha - \varepsilon_{\alpha'})\langle\psi_{\alpha'}\,|\,\delta\psi_\alpha\rangle, & n' \neq n,\ \boldsymbol{k}_{\|} = \boldsymbol{k}'_{\|} \end{cases} \tag{14}$$

where $\delta v \equiv v'\delta Q$ and $\delta\varepsilon_\alpha$ is the first-order change in ε_α. This result for the matrix element shows that both $\langle\psi_\alpha\,|\,v'\,|\,\psi_\beta\rangle$ and $\delta\psi_\alpha(\boldsymbol{r}_0)$ can be calculated from the two displaced configurations by $\pm\delta Q/2$ by using central differences and choosing phases of the wavefunctions such that $\langle\psi_\alpha(\delta Q)\,|\,\psi_\alpha(-\delta Q)\rangle \simeq 1$. In the wavefunction overlaps one should use, as in the calculation of the PDOS in eqn. (2), the states obtained by acting with $\hat{S}^{1/2}$ on the pseudo-states.[26]

III. Results and discussion

A. Chemisorption bond parameters and electronic structure

The first step is to determine the equilibrium geometry of the chemisorbed CO molecule on the (100) and (111) faces of Cu. We have restricted our geometry optimization to the experimentally determined configuration of CO adsorbed on the atop site perpendicular to the surface with the C atom coordinated to the Cu atom. A relaxation of perpendicular coordinates of the C and O distances and all the coordinates for the two outermost Cu layers for the (2 × 2) surfaces give C–O and C–Cu distances of 1.17 and 1.86 Å for both Cu(100) and Cu(111), which are in good agreement with the corresponding distances 1.15 and 1.9 Å for Cu(100) obtained by an analysis of low-energy electron diffraction data.[33] In the calculations of the electronic structure for the larger unit cells we have used these coordinates for the C and O atoms but on the unrelaxed slab. The calculated chemisorption energies are 0.70 and 0.77 eV for the p(2 × 2) structures on the (111) and (100) faces, respectively.

Table 1 Calculated vibrational energies for CO on a rigid Cu(100) surface. The mode patterns are schematically depicted by showing the relative phases of the motion of the molecule with the corresponding mode labels. The values within the parentheses are from experiments.

Mode	CO	$\hbar\Omega$/meV
ν_I	←→	265 (259)[a]
ν_M	←←	41 (43)[b]
ν_R	↑↓	31 (35)[b]
ν_T	↓↓	6.6 (3.5)[c]

[a] Ref. 34. [b] Ref. 35. [c] Ref. 36. All results have been obtained for the (2 × 2) surface unit cell with four layers.

For the p(2 × 2) structure of CO on the (100) surface of Cu, we have also determined the vibrational energies of the CO molecule on the rigid surface. The resulting energies of the vibrational modes, their schematic displacement fields and labels are shown in Table 1. For the two parallel modes of the CO molecule, the frustrated translational mode T and rotational mode **R**, we have diagonalized the dynamical matrix whereas, for the perpendicular modes, we have obtained the mode energies by calculating the energy for approximate displacement fields: a rigid displacement of the molecule for the frustrated translational mode M and a relative displacement of the C and O atoms with a fixed centre of mass for the internal stretch mode I. As shown in Table 1 the calculated mode energies are in good agreement with the experimental values, but this comparison is not entirely correct because the relatively low mass of the Cu atoms and the single coordination of the CO–Cu bind in the atop adsorption site introduce an upward energy shift for the modes *M* and *R* when the dynamic coupling to the substrate lattice is turned on.

We have analyzed the electronic structure of CO on the Cu surface using the calculated PDOS on molecular orbitals of the free molecule. In Fig. 1, we show the calculated PDOS on orbitals participating in the bonding of CO with Cu. The results for these PDOS for CO chemisorbed on Cu(100) are very similar to those for CO chemisorbed on Cu(111) and are not shown. We have also indicated the one-electron energies of the free molecular orbitals. We find that the one-electron energy, −29.3 eV, of the free 3σ orbital with respect to the vacuum level is essentially not shifted upon chemisorption, showing that the electrostatic shift of the level is negligible. The results for the PDOS show that the character of the molecular states survives, as expected for a weakly chemisorbed molecule such as CO on Cu. The largest changes occur for the HOMO orbital 5σ and the two-fold degenerate LUMO orbital 2π*. The 4σ orbital hybridizes slightly with the 5σ orbital and the 2-fold degenerate 1π orbital is largely unaffected, whereas the 5σ orbital hybridizes with the Cu d band, located in the energy region −5 to −3 eV, and overlaps with the Cu sp band and the 4σ orbital and shifts downward in energy by about 3 eV. The anti-bonding two-fold degenerate 2π* orbitals broaden dramatically into a partially filled resonance-like feature when overlapping with the sp band and hybridize with the Cu d band. The tails of the PDOS for the 2π* orbitals and 5σ orbital, below and above the Fermi-level, are consistent with the traditional Blyholder model[37] of chemisorption, involving donation from the 5σ orbital and back donation to the 2π* orbitals.

Here we are primarily interested in the nature of the 2π* resonance-like feature in the PDOS. As shown by the result for the PDOS on the 2π* orbitals for the p(4 × 4) structure of CO on Cu(111) in Fig. 2(a), the broadening is not an effect of the dispersion of the 2π* orbitals introduced by adsorbate–adsorbate interactions. Fig. 2(a) shows also that the PDOS is well converged with respect to the number of layers for Cu(111). In Fig. 2(b), we make a detailed comparison between

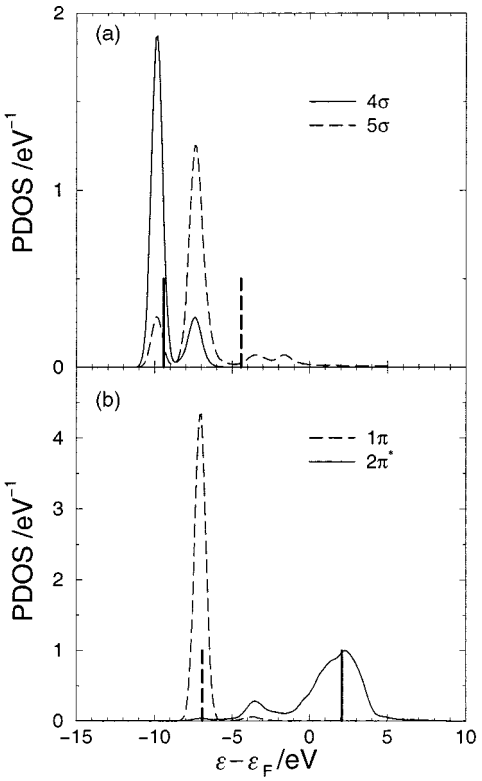

Fig. 1 Calculated PDOS of CO chemisorbed on Cu(111) in the p(2 × 2) structure. The projections are on molecular states with σ symmetry in (a) and π symmetry in (b) of the free molecule. The vertical lines are the positions of the free molecular states, slightly shifted in energy so that the energies of the 3σ states agree with the chemisorbed one. Note that both spin and orbital degeneracies are included. The PDOS have been broadened by a Gaussian with $\sigma = 0.5$ eV.

the PDOS for the 2π* orbitals for CO adsorbed on (111) and (100) faces. This comparison shows that both the half-widths, γ, at half-maximum and the positions, $\tilde{\varepsilon}^*_{2_\pi}$ of the center of the peaks are similar: $\gamma_{2\pi^*} \approx 1.15$ and 1.45 eV for the (111) and (100) face, respectively, and $\tilde{\varepsilon}_{2\pi^*} - \varepsilon_F \approx 1.9$ and 2.2 eV for the (111) and (100) faces, respectively. The slightly smaller value of $\gamma_{2\pi^*}$ for the (111) surface than for the (100) surface is probably an effect of the larger bandgap on the (111) surface than on the (100) surface. Note that part of the broadening is not inherent and derives from our Gaussian broadening of the PDOS. For CO on Pd(100), Delbecq and Sautet[38] obtained similar values for 2π*-derived resonance parameters from their density functional calculations.

Before attempting to make a direct comparison of the energy and width of the 2π-derived resonance state with experiments, we have to stress that DFT can, in principle, only describe ground-state properties so that the energies of unoccupied and occupied orbitals do not have a rigorous correspondence to excitation energies that are measured in experiments. One exception is the fact that the binding energy of the highest occupied Kohn–Sham orbital for the exact exchange-correlation functional is equal to its ionization energy.[39] Our calculated values of 14.2, 11.7 and 11.6 eV for the binding energies of the 4σ-, 1π- and 5σ-derived states of CO on Cu(100) are all downshifted by about 3 eV as compared to the corresponding ionization potentials 11.5, 8.5 and 8.5 eV measured by ultraviolet photoemission spectroscopy.[40] The 2π*-derived state has been investigated experimentally by inverse photoemission spectroscopy (IPS)[41] for CO in a c(2 × 2) structure on Cu(100) and by two-photon photoemission spectroscopy (2PPE)[42] for the $\sqrt{3} \times \sqrt{3}$ structure of CO on Cu(111). In IPS one measures the energy differences of the excited states of the system in the presence of an extra electron whereas 2PPE involves a two-step process in which an electron–hole pair is created in the first step by a photon from the pump pulse and an electron is

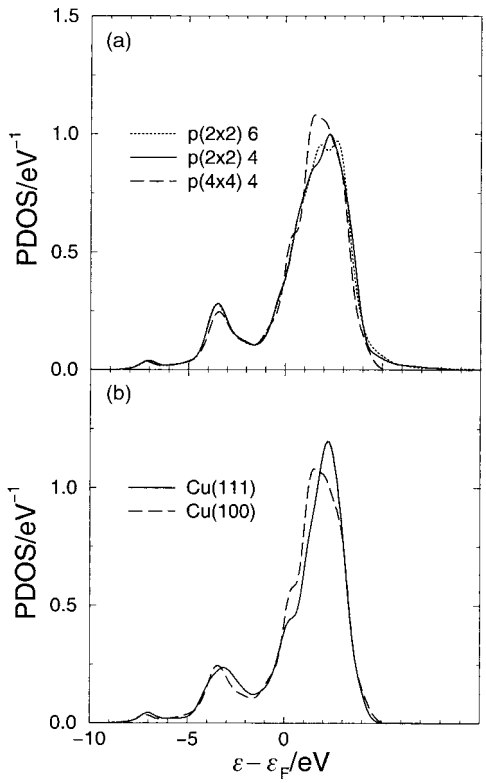

Fig. 2 Calculated PDOS on the $2\pi^*$ of CO chemisorbed on Cu(111) and Cu(100) in the p(4 × 4) structure. Same broadening as in Fig. 1 and the spin and orbital degeneracies are also included. (a) Variations of the PDOS with system size. (b) Surface dependence of the PDOS.

then emitted from this excited state by a second photon from the probe pulse. The IPS measurements identify two adsorbate-induced peaks at 2.6 and 3.6 eV above the Fermi level and the energy dependence of the cross-section suggests that the latter peak derives from a $2\pi^*$ level. In the analysis of the 2PPE measurements based on the photon polarization dependence, two peaks with π symmetry at 2.4 and 3.6 eV above the Fermi level are identified. From the sensitivity of these peaks to the adsorbate structure, the latter peak is shown to derive from the $2\pi^*$ level and its full-width at half-maximum (FWHM) is determined to be about 0.87 eV. These values for the energy and width differ significantly from the corresponding values of $\tilde{\varepsilon}_{2\pi^*} = 1.9$–$2.2$ and $2\gamma_{2\pi^*} =$ 2.3–2.9 eV that we obtain for the $2\pi^*$ resonance feature in the PDOS.

B. Elastic and vibrationally inelastic tunneling in STM

Here we present our calculated topographical STM images of CO chemisorbed on the (111) and (100) faces of Cu and vibrationally inelastic tunneling signals for some selected molecular modes and their spatial images. These results are also discussed in relation to available experimental data.

We find that the calculated topographical STM images, based on the LDOS at the Fermi level, have a large lateral extension and are sensitive to the size of the surface unit cell. In Fig. 3, we show contour plots of the calculated topographical images for the (3 × 3) and (4 × 4) structures of CO on Cu(100) at a distance of about 7 Å of the tip apex from the surface plane, z_0. For both structures the width of the image of CO is about 5 Å but the corrugations are somewhat different. In the (4 × 4) structure, the image is a protrusion with a maximum corrugation of 0.35 Å whereas for the (3 × 3) structure a depression of about 0.1 Å develops on top of the protrusion and the maximum corrugation for the (3 × 3) structure is about 0.17 Å. Such a depression in the image is

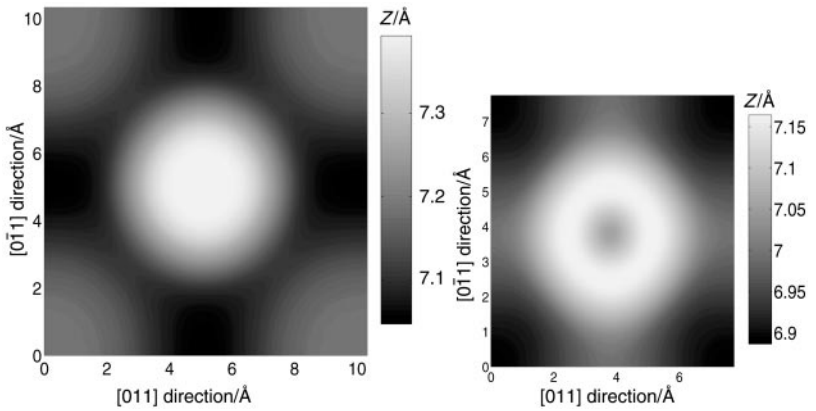

Fig. 3 Calculated topographical images of CO on Cu(100) for the p(4 × 4) and p(3 × 3) structures. The delta function has been broadened by a Gaussian with $\sigma = 0.25$ eV.

expected when the $2\pi^*$ orbitals contribute to the LDOS at the Fermi level because these orbitals have a node perpendicular to the surface. Increasing the distance z_0 from 7 to 9 Å decreases and smooths the overall corrugation. For the (4 × 4) structure the maximum corrugation decreases from 0.35 Å for $z_0 = 7$ Å to 0.15 Å for $z_0 = 9$ Å.

The sensitivity of the calculated STM image to the electronic structure is illustrated by comparing the image for CO on Cu(111), shown in Fig. 4, with the corresponding image for CO on Cu(100) in Fig. 3 at about the same average distance $z_0 \sim 7$ Å. A protrusion corresponding to the CO molecule is still found with a height of 0.08 Å. A depression is developed around the molecule, enhancing the "sombrero" shape of the image. The width of the protrusion is 4 Å (FWHM) and is about 1 Å less than the corresponding protrusion of CO on Cu(100).

Using the theory of vibrationally inelastic tunneling in Section III B, we find that the non-adiabatic coupling between the tunneling electrons and the vibration can be very efficient. In Table 2, we have summarized our results for the calculated maximum relative changes $\eta_{\mathrm{tot}}^{(\mathrm{max})}$, in tunneling conductance across some vibrational modes of CO chemisorbed on Cu(100) and Cu(111) for the p(4 × 4) structure. We have included results both from short-range electron vibration coupling in the sample based on eqn. (4), (6), (7) and (8) and from long-range dipole coupling based on eqn. (9). The latter contribution is essentially zero for the R modes and negligible for the T modes while it is dominant for the strongly infrared-active I modes. This result is in sharp

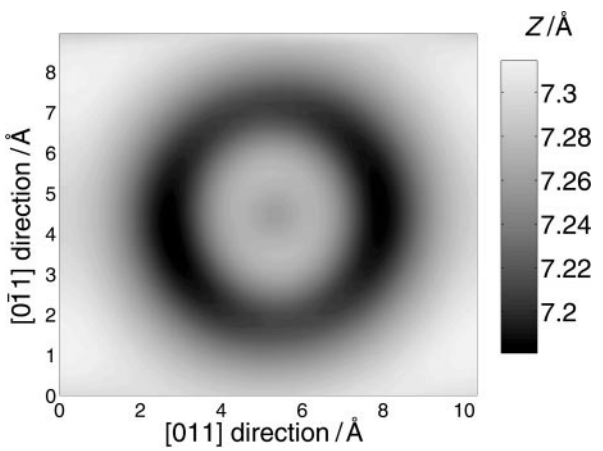

Fig. 4 Calculated topographical image of CO on Cu(111) for the p(4 × 4) structure. Same broadening function as in Fig. 3.

Table 2 Calculated relative changes in tunneling conductance, η, across some selected modes of CO adsorbed on Cu(100) or Cu(111). The calculated efficiencies are the values at maximum absolute value and correspond to $\sigma = 0.4$ eV while the values within the parentheses correspond to $\sigma = 0.25$ eV. All results have been obtained for the (4 × 4) surface unit cells

Mode	$\eta_{tot}^{(max)}$ (%)	$\eta_{inel}^{(max)}$ (%)	$\eta_{el}^{(min)}$ (%)	$\eta_{dip}^{(max)}$ (%)
Cu(100)				
ν_I	0.50(0.42)	0.64(0.79)	−0.15(−0.41)	1.3
ν_R	17.6(23.8)	19.3(25.6)	−1.6(−2.0)	0.0
Cu(111)				
ν_M	2.3(3.5)	2.9(4.2)	−0.56(−0.67)	0.08
ν_R	14.8(11.9)	17.1(15.2)	−2.2(−5.0)	0.0

contrast to the case of short-range coupling in the sample where the efficiences $\eta_{tot}^{(max)}$ are very large for the R modes and small for the I modes. Note that the two-fold degeneracy of the R modes makes the efficiencies a factor of two larger. The results for CO chemisorbed on the Cu(100) and Cu(111) faces show the same trends and are similar in magnitude. We find that the results for $\eta_{tot}^{(max)}$ are rather weakly dependent on the broadening, giving us confidence in our calculational procedure, but the large size of the systems, slabs with a (4 × 4) surface unit cell and 4 layers, have prohibited us from performing an investigation of the sensitivity of the results with respect to the number of layers.

In Table 2, we have also given results for the maximum magnitudes of the positive inelastic contributions, $\eta_{inel}^{(max)}$, and of the negative elastic contributions, $\eta_{el}^{(min)}$, to the vibrationally inelastic tunneling efficiencies. Note that the maximum magnitudes of η_{inel} and η_{el} are not necessarily attained at the same lateral positions of the tip apex. For the R and T modes, η is dominated by the inelastic contribution whereas for the I modes $\eta_{el}^{(min)}$ is comparable to $\eta_{inel}^{(max)}$ but in all cases $\eta_{tot}^{(max)}$ is positive. As shown by the result in eqn. (8), when the inelastic contribution η_{inel} dominates over η_{el}, the vibrationally inelastic tunneling efficiency is determined by the change of tunneling amplitude with vibrational coordinate.

We have also investigated the spatial distribution of the vibrationally inelastic efficiency. In Fig. 5, we have plotted a profile of η_{tot} for the R modes of CO on Cu(100) and Cu(111). The calculated profiles for these two surfaces are very similar and show a maximum at the molecule and a

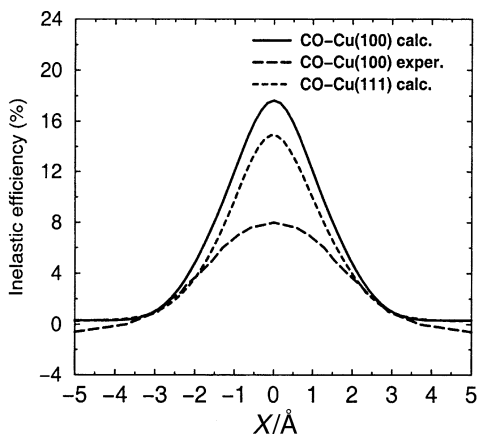

Fig. 5 Profiles of vibrational inelastic images of the frustrated rotation of CO on Cu. The (——) and (– –): calculated results for the (100) and (111) faces of Cu, respectively, (— · —) experimental result for d^2I/dV taken from Lauhon and Ho,[43] scaled to the observed value of 8% for $\Delta\sigma/\sigma$. The profiles for the (111) and (100) surfaces are along the [1$\bar{1}$0] and [001] directions, respectively with the origin at the adsorption site. The delta function has been broadened by a Gaussian with $\sigma = 0.4$ eV.

FWHM of about 2.3 and 2.8 Å for the (111) and (100) faces, respectively, about 2 Å narrower than the constant LDOS image.

A general problem when comparing calculated STM images with experiments is that the images are tip dependent and that the state of the tip is not very well-characterized. In the case of the STM image of CO chemisorbed on Cu(100), Lauhon and Ho find a circular depression of about 0.2 Å with a FWHM of about 5.7 Å at a bias of 0.036 mV and a tunneling current of about 1 nA,[43] whereas for an etched tip, they find a protrusion of about 0.5 Å with a FWHM of about 2.4 Å at a bias of 0.1 V and tunneling current of 1 nA.[44] We have not attempted to calculate any absolute values of the tunneling conductances because this calculation requires certain unknown parameters that are, usually, at best educated guesses, such as the radius of curvature of the tip and its density of states. However, our average value of about 7 Å for z_0 is in the experimental range of distances[45] where TH theory is applicable.[46]

We find an overall agreement of the calculated η_{tot} with the measured $\Delta\sigma/\sigma$ for vibrational modes of CO chemisorbed on Cu(100) by Lauhon and Ho.[43] As in the experiments, we find that the **R** mode gives the dominant signal and that the signal from the I mode is weak. The calculated value for η for the **R** mode in Table 2 is about twice that of the measured value for $\Delta\sigma/\sigma$ of about 8%. In the case of the I mode, we find that η_{tot} is dominated by inelastic dipole scattering and its calculated value of 1.8% is close to the measured value of about 1.5% for $\Delta\sigma/\sigma$. As shown in Fig. 5, the calculations can also account for the observed image of the vibrationally inelastic signal. The shape of the spatial image of the calculated η_{tot} for the **R** mode is in good agreement with the rescaled experimental image of d^2I/dV^2, recorded by Lauhon and Ho[43] at a bias corresponding to the vibrational energy. Finally, we would like to mention that recent experiments by Moresco *et al.*[47] have also established that the **R** mode gives a dominant signal in vibrationally inelastic tunneling of CO on Cu(211).

C. Vibrational damping rates

Here we present our calculated vibrational damping rates for some selected modes of CO adsorbed on the (111) and (100) faces of Cu and discuss them in relation to experimental data.

In Table 3, we have summarized our results for damping rates, γ_{eh}, for some vibrational modes of CO on Cu by excitation of electron–hole pairs. The relatively weak dependence of the calculated γ_{eh} on the broadening and the number of layers shows that the calculated values are basically converged and gives us confidence in our calculational scheme. The dependence of the damping rates on the size of the surface unit cell is probably not significant at the present level of accuracy. We are calculating the damping rate of a collective vibrational mode at the Γ point in the surface Brillouin zone so a dependence on the surface structure might be present, at least for high coverages, but the present result indicates that our results for the p(2 × 2) structures are close to the result for an isolated molecule.

Table 3 Calculated vibrational damping rates for some selected modes of CO adsorbed on Cu(100) or Cu(111). The calculated damping rates, γ are shown as a function of the broadening σ and surface structure. The values within the parentheses correspond to a 6 layer slab and all other values are obtained for a 4 layer slab

	$\gamma_{eh}/10^{12}$ s^{-1}		
Mode	$\sigma = 0.2$ eV	$\sigma = 0.3$ eV	$\sigma = 0.4$ eV
p(2 × 2)CO–Cu(100)			
ν_I	0.53(0.57)	0.57(0.50)	0.58(0.48)
p(4 × 4)CO–Cu(100)			
ν_I	0.76	0.70	0.63
ν_R	0.47	0.52	0.52
p(4 × 4)CO–Cu(111)			
ν_M	0.14	0.11	0.11
ν_R	0.17	0.31	0.39

We find a significant variation of the γ_{eh} over the various vibrational modes and some dependence on the crystal face. The largest value of γ_{eh} is attained for the I mode whereas γ_{eh} has its smallest value for the M mode. The results for γ_{eh} of the R mode indicate that γ_{eh} is somewhat smaller on the (111) face than on the (100) face. The results for the damping rates obtained by Head-Gordon and Tully[32] using Hartree–Fock and a cluster representation of CO on Cu are similar to our results except that they find the damping rate for the M mode to be an order of magnitude smaller than our result.

We find also that our calculated γ_{eh} are in good agreement with experimental data. The most direct measurement of damping rates comes from real-time measurements using picosecond pump–probe pulses, whereas less direct measurements come from an analysis of Fano lineshapes in infrared reflection absorption spectroscopy (IRAS) but gives directly the electron–hole pair contribution. The pump–probe measurements by Morin *et al.*[48] of the I mode of CO in a c(2 × 2) structure on Cu(100) resulted in a value of about 0.5×10^{12} s^{-1} for the damping rate, which supports the early results obtained from infrared lineshape measurements by Ryberg.[49] This value is in excellent agreement with our calculated value of about $(0.5–0.6) \times 10^{12}$ s^{-1}. The analysis of the Fano lineshapes of the R mode of CO suggested the values 0.33×10^{12} s^{-1} and 1×10^{12} s^{-1} for γ_{eh} of the c(2 × 2) and $\sqrt{3} \times \sqrt{3}$ structure of CO on Cu(100) and Cu(111), respectively. In particular, the value for CO on Cu(100) is in good agreement with our calculated value for the R mode in Table 3. Thus this favourable comparison gives additional support for our theoretical approach to electron–vibration coupling in the excitation of electron–hole pairs in vibrational damping.

D. Some implications for tip-induced desorption

Here we discuss our results for the 2π-derived resonance state, vibrationally inelastic tunneling rates and vibrational damping rates in relation to recent work on tip-induced desorption of CO on Cu.

The observed desorption of individual CO molecules on Cu(111) by single electrons tunneling from a STM tip at a bias exceeding 2.4 V was interpreted as being induced by a transient occupation of a 2π*-derived level.[7] In their analysis of the data in terms of a 1D model for the desorption coordinate using a Menzel–Gomer–Redhead-like resonance model proposed by Gadzuk,[50] they concluded from the observed isotope effect and 2PPE measurements of the resonance width of the 2π*-derived level that the tip-induced desorption probability of about 5×10^{-9} per tunneling electron can be accounted for by a potential slope of the excited state of about 1 eV $Å^{-1}$ and a fraction in the range 0.01–4% of the tunneling current passing through the resonance.

Our calculations of vibrationally inelastic tunneling and vibrational damping rates suggest that this picture of the mechanism for tip-induced desorption is incomplete. Our calculated values for η_{inel} give the probability for a tunneling electron with an energy above the vibrational threshhold to excite an vibration and show that the R mode is most efficiently excited with a probability as large as 10%. Note that the trend of $\eta_{inel}^{(max)}$ over various modes has no correlation with γ_{eh}. We find that the excitation probabilities $\eta_{inel}^{(max)}$ for the M and I modes cannot simply be understood in a NA model for resonance coupling through a 2π-derived level although we find that this model describes the electron–vibration coupling in the electron–hole pair damping of the I mode.

In the NA model for the vibrational damping rate, γ_{eh}, presented in Section II C, γ_{eh} is determined by the density of states, $\rho_a(\varepsilon_F)$, projected on the molecular 2π* orbital and the slope, $\partial\varepsilon_a/\partial q$, of the average resonance energy. From our calculated PDOS on this orbital for CO in the p(2 × 2) structure on Cu(100) as a function of vibrational coordinate, we find that $\rho_a(\varepsilon) \approx 0.095$ eV^{-1} for a single 2π* orbital and single spin, and $\partial\varepsilon_a/\partial q \approx 2.5$ eV $Å^{-1}$ resulting in value of about 0.66×10^{12} s^{-1} for γ_{eh}. This value is very close to our calculated value in Table 3 using the full expression in eqn. (10). Thus this comparison gives strong support for the resonance model of the electron–vibration coupling for γ_{eh} of the I mode and also for the original application of this model by Persson and Persson.[17] However, in the latter application the parameters were determined indirectly from experiments.

In the case of vibrationally inelastic tunneling, the NA model presented in Section II C is not able to account for the calculated $\eta_{inel}^{(max)}$. First we make the most favourable assumption that all electrons tunnel through the 2π*-derived level, that is, the LDOS is assumed to be dominated by

the contribution from the 2π* orbital. From our calculated values of 2.5 eV $Å^{-1}$, 2.2 eV, and 1.45 eV for $\partial\varepsilon_a/\partial q$, $\Delta\varepsilon_a$ and γ_a for the 2π*-derived resonance-like feature of CO on Cu(100), we obtain, based on eqn. (11), a value of about 0.1% for $\eta_{inel}^{(max)}$, which is about a factor of 5 smaller than the calculated value of 0.5%. In the case of the M mode, the discrepancy is even larger than for the I mode because we find that $\partial\varepsilon_a/\partial q$ about a factor of four smaller for the M mode than for the I mode and the calculated strength is about a factor of six larger for the M mode than for the I mode. We believe that this resonance model misses an important mechanism for electron–vibration coupling in tunneling, suggested by eqn. (8), that involves the change of tunneling amplitude by deformation of tails of the one-electron wavefunctions with respect to the vibrational coordinate. More work is needed to elucidate the role of this mechanism in creating the excitations of the bond beyond the first excited vibrational state that are necessary to break the bond by single tunneling electrons.

IV. Summary and concluding remarks

We have performed a density functional study of the electronic structure, images and vibrationally inelastic tunneling in the STM, and vibrational damping rates of CO on the (111) and the (100) faces of Cu, with the objective of gaining a better understanding of the nature of the electron–vibration coupling in tunneling-current-induced bond excitation and breaking at surfaces. The calculation of the STM images, the relative changes in tunneling conductance across vibrational thresholds and their real space images were based on TH theory and its generalization to the interaction of tunneling electrons with an adsorbate vibration. The non-adiabatic electron–vibration coupling was treated by perturbation theory. The one-electron wavefunctions and electron–vibration couplings were calculated in a super-cell geometry using a plane-wave and pseudopotential method. The electronic structure of the chemisorbed molecule was characterized by calculating PDOS on molecular orbitals.

Of particular interest in this study is the character of the 2π*-derived state and its effect on the electron–vibration coupling. The unoccupied 2π*-orbital turns into a broad and partially filled resonance-like feature in the projected density of states when interacting with the sp and d bands of Cu. The energy, position and width of this feature are very similar on the (111) and (100) faces of Cu but they differ significantly from the position and width suggested by IPS and 2PPE spectroscopic measurements. The calculated vibrational damping rate for the internal stretch mode supports the NA model 2π*-derived for the electron–vibration coupling. The calculated vibrational damping rates are in good agreement with available experimental data. We find that this resonance model is not able to describe our calculated vibrational excitation probabilities in inelastic tunneling and gives too small probabilities. We believe that such a resonance model misses an important mechanism for vibrational excitation in tunneling that involves the change of tunneling amplitude by deformation of tails of the one-electron wave-functions with vibrational coordinate. The calculated relative changes in tunneling conductance across vibrational thresholds and their real space images are in agreement with available experimental data and do not show a simple correlation with calculated vibrational damping rates. Thus our results indicate that simple resonance models that involves an electron–vibration coupling only through the slope of the resonance energy do not completely describe tip-induced bond excitation and breaking.

Acknowledgements

We thank Lincoln Lauhon and Wilson Ho for sharing their experimental data with us prior to publication. We are grateful for support from the Swedish Natural Science Research Council (NFR) and the European Commission's TMR Programme, Contract #ERBFMRXCT970146, Atomic/Molecular Manipulations. The allocations of computer resources by UNICC at Chalmers and PDC in Stockholm are also acknowledged.

References

1 J. K. Gimzewski and C. Joachim, *Science*, 1999, **283**, 1683.
2 T. C. Shen, C. Wang, G. C. Abeln, J. R. Tucker, J. W. Lyding, Ph. Avouris and R. E. Walkup, *Science*, 1995, **268**, 1590.

3 K. Stokbro, C. Thirstrup, M. Sakurai, U. Quaade, Ben Yu-Kuang Hu, F. Perez-Murano and F. Grey, *Phys. Rev. Lett.*, 1998, **80**, 2618.
4 B. C. Stipe, M. A. Rezaei, W. Ho, S. Gao, M. Persson and B. I. Lundqvist, *Phys. Rev. Lett.*, 1997, **78**, 4410.
5 L. Lauhon and W. Ho, *Phys. Rev. Lett.*, 2000, **84**, 1527.
6 D. M. Eigler, C. P. Lutz and W. E. Rudge, *Nature*, 1991, **352**, 600.
7 L. Bartels, G. Meyer, K.-H. Rieder, D. Velic, E. Knoesel, A. Hotzel, M. Wolf and G. Ertl, *Phys. Rev. Lett.*, 1998, **80**, 2004.
8 H. J. Lee and W. Ho, *Science*, 1999, **286**, 1719.
9 B. C. Stipe, M. A. Rezaei and W. Ho, *Science*, 1998, **279**, 1907.
10 B. C. Stipe, M. A. Rezaei and W. Ho, *Phys. Rev. Lett.*, 1998, **81**, 1263.
11 B. C. Stipe, M. A. Rezaei and W. Ho, *Science*, 1998, **280**, 1732.
12 S. Gao, M. Persson and B. I. Lundqvist, *Solid State Commun.*, 1992, **84**, 271.
13 M. Brandbyge and P. Hedegård, *Phys. Rev. Lett.*, 1994, **72**, 2919.
14 G. P. Salam, M. Persson and R. E. Palmer, *Phys. Rev. B*, 1994, **49**, 10655.
15 S. Gao, M. Persson and B. I. Lundqvist, *Phys. Rev. B*, 1997, **55**, 4825.
16 J. W. Gadzuk, *Phys. Rev. B*, 1991, **44**, 13466.
17 B. N. J. Persson and M. Persson, *Solid State. Commun.*, 1980, **36**, 175.
18 B. N. J. Persson and A. Baratoff, *Phys. Rev. Lett.*, 1987, **59**, 339.
19 N. Lorente and M. Persson, *Phys. Rev. Lett.*, submitted.
20 We used an optimized version 1.30 of DACAPO of CAMP, DTH, Denmark.
21 J. P. Perdew, J. A. Chevary, S. H. Vosko, K. A. Jackson, M. R. Pederson, D. J. Singh and C. Fiolhais, *Phys. Rev. B*, 1992, **46**, 6671.
22 L. Bengtsson, *Phys. Rev. B*, 1999, **59**, 12301.
23 For the (2 × 2), (3 × 3) and (4 × 4) surface unit cells, we used 36, 16 and 9 k points in the surface Brillouin zone, respectively.
24 (*a*) J. Tersoff and D. R. Hamann, *Phys. Rev. Lett.*, 1983, **50**, 1998; (*b*) J. Tersoff and D. R. Hamann, *Phys. Rev. B*, 1985, **31**, 805.
25 D. Vanderbilt, *Phys. Rev. B*, 1990, **41**, 7892.
26 The calculation of $\hat{S}^{1/2}$ is described in ref. 28.
27 W. Sacks, S. Gauthier, S. Rousset, J. Klein and M. A. Esrick, *Phys. Rev. B*, 1987, **36**, 961.
28 N. Lorente, M. Persson and L. Bengtsson, to be submitted.
29 C. Caroli, R. Combescot, P. Nozieres and D. Saint-James, *J. Phys. C*, 1972, **5**, 21.
30 B. N. J. Persson and J. E. Demuth, *Solid State Commun.*, 1986, **57**, 769.
31 B. Hellsing and M. Persson, *Phys. Scr.*, 1984, **29**, 360.
32 (*a*) M. Head-Gordon and J. C. Tully, *Phys. Rev. B*, 1992, **46**, 1853; (*b*) M. Head-Gordon and J. C. Tully, *J. Chem. Phys.*, 1992, **96**, 3939.
33 S. Andersson and J. B. Pendry, *Phys. Rev. Lett.*, 1979, **44**, 363.
34 S. Andersson, *Surf. Sci.*, 1979, **89**, 477.
35 C. J. Hirschmugl, G. P. Williams and F. M. Hoffmann, *Phys. Rev. Lett.*, 1990, **65**, 480.
36 B. F. Mason, R. Caudano and B. R. Williams, *Phys. Rev. Lett.*, 1981, **47**, 1141.
37 G. Blyholder, *J. Phys. Chem.*, 1964, **68**, 2772.
38 F. Delbecq and P. Sautet, *Phys. Rev. B*, 1999, **59**, 5142.
39 J. P. Perdew, R. G. Parr, M. Levy and J. L. Balduz, *Phys. Rev. Lett.*, 1982, **49**, 1691.
40 J. L. Pascual, L. G. M. Pettersson and H. Ågren, *Phys. Rev. B*, 1997, **56**, 7716.
41 K.-D. Tsuei and P. D. Johnson, *Phys. Rev. B*, 1992, **45**, 13287.
42 M. Wolf, A. Hotzel, E. Knoesel and D. Velic, *Phys. Rev. B*, 1999, **59**, 5926.
43 L. J. Lauhon and W. Ho, *Phys. Rev. B*, 1999, **60**, R8525.
44 L. J. Lauhon, personal communication.
45 S. Heinze, S. Blügel, R. Pascal, M. Bode and R. Wiesendanger, *Phys. Rev. B*, 1998, **58**, 16432.
46 N. D. Lang, *Phys. Rev. B*, 1988, **37**, 10395.
47 F. Moresco, G. Meyer and K.-H. Rieder, *Mod. Phys. Lett. B*, 1999, **13**, 709.
48 M. Morin, N. J. Levinos and A. L. Harris, *J. Chem. Phys.*, 1992, **96**, 3950.
49 R. Ryberg, *Phys. Rev. B*, 1985, **32**, 2671.
50 J. W. Gadzuk, *Surf. Sci.*, 1995, **342**, 345.